

pubs.acs.org/acsaelm Article

Facile Synthesis and Single-Switch Antenna Application of Germanium-Doped Vanadium Dioxide

Roberto Prado-Rivera, Cheng-Yu Lai, Mujtaba Ali Haqqani Mohammed, Chen-Yu Chang, Faizan Syed, and Daniela R. Radu*



Cite This: https://doi.org/10.1021/acsaelm.3c00498



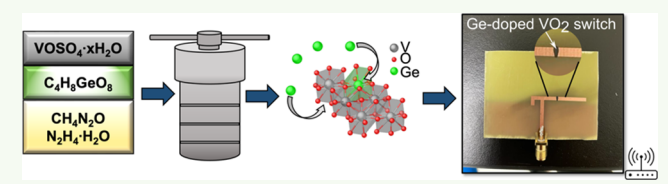
ACCESS I

Metrics & More

Article Recommendations

SI Supporting Information

ABSTRACT: Materials that undergo a phase transition from metallic to insulating, or metal—insulator transition (MIT), materials have become widely popular for their potential in emerging technologies due to their drastic conductivity change upon transitioning. Notable among the MIT materials is vanadium dioxide (VO₂), and ongoing efforts are focused on tuning its MIT phase transition temperature (TMIT). In this report, VO₂



germanium-doped nanoparticles with various germanium dopant levels were synthesized via a hydrothermal route and used in a simple single-switch antenna. Powder X-ray diffraction (XRD) analysis shows a monoclinic phase (M1) for both the pure and Gedoped VO₂ nanomaterials at room temperature, with no change in the diffraction pattern in the Ge-doped samples at low doping percentages; the M1 phase for both pure and Ge-doped VO₂ was further confirmed by Raman spectroscopy. Energy-dispersive X-ray spectroscopy (EDS) showed Ge uniformly distributed in the nanomaterials. The nanoparticles' morphology, imaged by field-emission scanning electron microscopy (FE-SEM) and transmission electron microscopy (TEM), reveals a morphology change from nanoparticles to nanosheets with increased dopant concentration. Ge-doped VO₂ nanoparticle dispersions were used to print a single switch in an antenna solely obtained through a facile printing process. A vector network analyzer used to characterize the antenna performance showed that the germanium doping successfully changed the transition temperature of the material, demonstrating the capability of controlling the antenna operation frequencies as a function of material doping. Density functional theory (DFT) shows that substituting Ge into a V site of the crystal structure distorts the lattice and reduces the band gap at high doping percentages. These results provide insight into the potential of smart switches fabricated from Ge-doped VO₂.

KEYWORDS: VO2, nanoparticle inks, metal-insulator transition, printed electronics, antenna

1. INTRODUCTION

Metal-insulator transition (MIT) materials have long attracted researchers' attention due to their ability to change their properties via a reversible phase change from metallic to insulating materials. This transition could be caused by changes in the crystal symmetry that alter the electronic band structure. Lattice distortions, for example, can increase the number of atoms/molecules per primitive cell, creating extra energy gaps or band splitting when the symmetry is lowered.1 A similar phenomenon can be seen with antiferromagnetic ordering: as the number of atoms/molecules per magnetic primitive cell increases, extra energy gaps are formed.² In both instances, the electrons are assumed to be noninteracting. Phase transitions can also be rationalized by considering the strong Coulomb interactions between electrons or electron-electron correlation. Under the assumption of noninteracting electrons, overlapping atomic orbitals at a site within the lattice could form a single band occupied by a spin-up and spin-down electron pair. However, considering the case in which the electrons interact via a repulsive Coulomb force, the single band can split into two, forming a Mott insulator.

Vanadium oxides such as VO, V_2O_3 , V_3O_5 , and VO_2 have long held the attention of researchers for their MIT behavior. $^{1,3-10}$ The transition temperature of VO_2 is approximately $T_{\rm MIT}\approx 340$ K, providing an accessible way to manipulate the material properties near room temperature. At this temperature, the crystal structure of VO_2 changes from a low-temperature, insulating, monoclinic phase (M1; space group $P2_1/c$) to a high-temperature, metallic, rutile phase (R; space group $P4_2/mnm$). This transition is accompanied by a significant change in resistivity and increased crystal symmetry. By utilizing this phase transition, VO_2 has found usage in "smart" technology such as thermochromic coatings and thin films, 12,13 gas sensing, 14 and batteries. 15

As the MIT occurs rapidly, VO₂ has found use in antenna applications for fast frequency switching in reconfigurable

Received: April 17, 2023 Accepted: May 23, 2023



antennas and radiofrequency-based applications. $^{16-18}$ Since the MIT can be triggered without an electrical bias, VO_2 switches can be easily integrated into systems without the need for complex electrical components. Furthermore, advances in inkjet printing demonstrate that VO_2 -based electronic inks can produce sub-millimeter-sized switches. This is desirable for antenna applications in limited spaces, such as commercial smartphones and telecommunication devices.

The transition temperature must be tuned based on the device application. For example, it is desirable to modulate $T_{\rm MIT}$ to commercialize smart windows that block infrared rays or to reduce energy consumption when cooling buildings. ^{12,13,21} One way of tuning $T_{\rm MIT}$ is doping different elements into its crystal structure. This reduces the electronic and structural differences between the M1 and R phases, thereby reducing $T_{\rm MIT}$. Substitution of V⁴⁺ with elements of higher valency and large ionic radii has been found to significantly reduce $T_{\rm MIT}$ by acting as electron donors. The best-known example is W, with a valency of 6⁺, ^{22,23} which was reported to lower $T_{\rm MIT}$ by 22–25 K/at % in thin films, ^{23,24} 48–56 K/at % in nanowires, ²⁵ and 18.4 K/at % in nanowires.

On the other hand, $T_{\rm MIT}$ can be increased by doping with lower-valency elements to stabilize an intermediate phase, typically the monoclinic phase M2 (space group C2/m). Krammer et al. achieved an increase of 4.5 K to the transition temperature through Si-doped VO₂. The study was geared toward preventing overheating in solar thermal collectors. An impressive increase of $T_{\rm MIT}$ (up to 407 K) was demonstrated in Fe-doped VO₂ and ascribed to structural defects created by substituting V with Fe in the V–V zigzag chains of the M2 phase. Interestingly, Cr-doped VO₂, which can achieve a 4.7 K/at % increase in $T_{\rm MIT}$, was reported to transform into an orthorhombic lattice similar to, but distinct from, the M2 phase. ²⁸

Compared to the literature on decreasing $T_{\rm MIT}$, doping to raise $T_{\rm MIT}$ is relatively underrepresented. One elemental dopant that has recently received attention is Ge. Ge-doped VO₂ was reported²⁹ to increase the transition temperature, confirmed as possessing a $T_{\rm MIT}$ of 358 K at 5 at %. Manipulating the transition temperature can depend on the fabrication techniques employed, as hinted by Ertas Uslu et al., who reported changes in the reflectivity of their thin films closer to 50 °C, below the $T_{\rm MIT}$ of pure VO₂. Elevated values of $T_{\rm MIT}$ are possible if the doping amount is increased, with the highest recorded being 369 K at 5.9 at % for Ge doping. Computational simulations support these results, with calculations predicting an increase of 1.32 K/at %. 32

Herein, VO₂(M1) doped with germanium is synthesized using a hydrothermal process followed by high-temperature annealing to produce nanoparticle powders. The Ge-doped VO₂ powders are characterized by XRD, confirming their monoclinic phase and demonstrating the minor effects of the Ge dopant on the structure. Scanning electron microscopy demonstrated the nanoparticle morphology of the synthesized powders, and energy-dispersive X-ray spectroscopy showed Ge uniformly incorporated into the doped samples. Fourier transform infrared (FTIR) spectroscopy with an attenuated total reflectance (ATR) attachment showed no residual organic ligands from the hydrothermal synthesis. Nanoparticle inks were prepared from the pure and Ge-doped VO₂ powders and patterned-printed as switches in a proof-of-concept antenna. The performance of the antenna using the Ge-

doped VO_2 switches, evaluated with a vector network analyzer, shows changes in the operating frequency upon heating, due to the MIT, when compared with the control using the undoped VO_2 switches.

2. MATERIALS AND METHODS

- **2.1. Materials.** All chemicals used in the experiment were used as received without further purification. Vanadyl (IV) sulfate hydrate (VOSO₄:xH₂O, 17–23% V) and urea (CH₄N₂O, 99.5%) were purchased from Acros Organics. Hydrazine monohydrate (H₂NNH₂· H₂O, >98%) was purchased from Alfa Aesar. Nanopure water (ASTM Type 1) was purchased from LabChem. Terpineol (C₁₀H₁₈O, 98%) was purchased from Alfa Aesar. Ethyl cellulose (EC; 4 cP, 5% in toluene/ethanol 80:20, 48% ethoxyl) was purchased from Sigma-Aldrich. Glycolic acid (99%) and diethyl ether (99%) were purchased from Sigma-Aldrich, GeO₂ (99.99%) was purchased from MSE Supplies, and the PCB etchant solution was purchased from CAIG Laboratories, Inc.
- **2.2. Preparation of Diaquabis(glycolato-O,O") Germanium-(IV).** Diaquabis(glycolato-O, O") germanium(IV) ($C_4H_8GeO_8$), hereafter called Ge-Gly, was prepared by a modified method by Chiang et al. and Liu et al. ^{33,34} Generally, 2 g of GeO_2 was dissolved in 100 mL of water with 6 g of glycolic acid. The mixture was then refluxed at 120 °C for 4 h, producing a final solution that was colorless and transparent. Afterward, the solvents were removed using a rotary evaporator. Diethyl ether was added to promote crystallization. The resulting white crystalline powder was collected through vacuum filtration and dried overnight in a vacuum oven.
- 2.3. Preparation of Ge-Doped VO₂ Powders. VO₂ was produced by a hydrothermal synthesis route followed by hightemperature annealing, a method previously shown to produce phase-pure nanoparticles. 19,35,36 In a typical experiment, VOSO₄: α H₂O (1.228 g, 7.534 mmol) and urea (0.900 g, 14.985 mmol) were mixed in 70 mL of nanopure water. Once all the precursors dissolved and the solution became clear blue, 225 μL of 10% aqueous hydrazine monohydrate was added dropwise into the solution and kept under stirring for 10 min. Ge-Gly in predetermined amounts corresponding to the targeted doping percentage was added next to the solution. The final solution was transferred to a 100 mL Teflon-lined stainless-steel autoclave and placed in an oven at 240 °C for 6 h. The autoclave was allowed to cool to room temperature before the precipitate was collected and washed three times with a 1:1 (v/v) solution of nanopure water and isopropanol. The product was then dried under vacuum at 60 °C overnight. The dried product was annealed twice, first under vacuum at 300 °C for 3 h to yield nanoparticles and then under argon gas flow at 700 °C for 45 min to improve crystallinity.
- **2.4. Preparation of Ge-Doped VO₂ Nanoparticle Inks.** A solution of ethanol and terpineol was first prepared at a 1: 0.1 (v/v) ratio at room temperature. The Ge-doped VO₂ powder (500 mg) was dispersed in 2.0 mL of the prepared solution, followed by the addition of an ethyl cellulose solution (5% in toluene/ethanol 80:20 v/v), and sonicated for 2.5 h. Following sonication, the ink was then kept under stirring for 2 days.
- 2.5. Fabrication of a Single-Switch Antenna with the Ge-Doped VO₂ Switch. Single-switch antennas were fabricated via laser engraving on a double-sided copper-clad laminate FR4 PCB board, followed by precise deposition of nanoparticle inks. First, the PCB board was covered in a layer of protective enamel (Figure S1A). Next, the antenna design, adapted from Vaseem et al.,³⁷ was sketched on the electronic computer-aided design software Easy EDA and imported into the open-source laser engraving software, LaserGRBL, which operates the laser engraver (Ortur Laser Master 2 Pro, 3000 mm· min⁻¹, 5.5 W laser power, $\lambda = 450$ nm). The PCB board's enamelcoated side was engraved so that the antenna design was not exposed to the laser (Figure S1B). Following engraving, the PCB board was immersed in a commercial PCB etchant solution containing water, ferric chloride, ferrous chloride, and hydrochloric acid (CAIG Laboratories, Inc), etching away exposed copper cladding for 30 min (Figure S1C). The PCB board was rinsed with nanopure water,

ACS Applied Electronic Materials

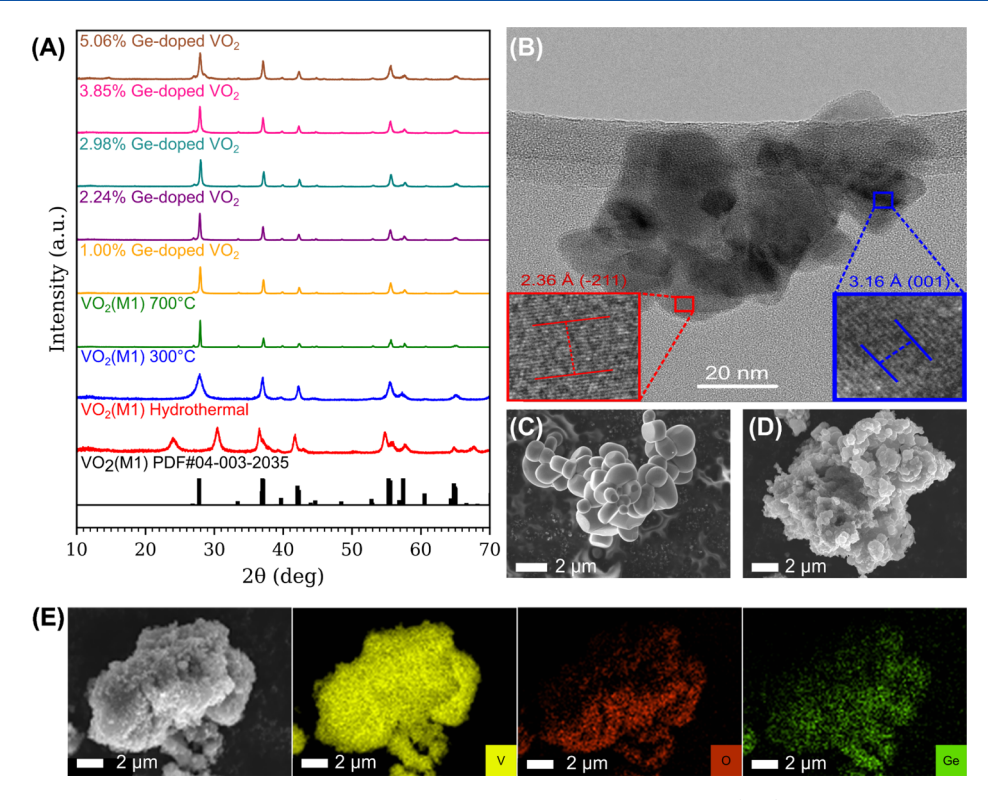


Figure 1. (A) Powder XRD pattern for Ge-doped VO₂ at different doping amounts: pure VO₂(M1) after hydrothermal synthesis (red), pure VO₂(M1) annealed at 300 °C under vacuum (blue), and pure VO₂(M1) annealed at 700 °C under argon (green); all Ge-doped VO₂ samples spectra are recorded postannealing at 700 °C under argon: 1.00% Ge-doped VO₂ (yellow), 2.24% Ge-doped VO₂ (purple), 2.95% Ge-doped VO₂ (teal), 3.85% Ge-doped VO₂ (pink), and 5.06% Ge-doped VO₂ (brown); bottom—the reference pattern for VO₂(M1) from the ICDD PDF4 database (PDF #04-003-2035). (B) TEM image of 3.85% Ge-doped VO₂. (C) FE-SEM image of synthesized VO₂(M1). (D) FE-SEM image of 3.85% Ge-doped VO₂. (E) SEM-EDS mapping of 3.85% Ge-doped VO₂. All TEM and SEM images are for samples annealed at 700 °C under argon.

and excess enamel was removed postetching using acetone. Finally, nanoparticle inks were deposited using a Voltera V-One PCB printer and dried overnight (Figure S1D).

2.6. Computational Details. The geometry optimization and electronic structure calculations of pure and Ge-doped VO₂ were performed using density functional theory (DFT) as implemented in the Vienna ab initio simulation package ^{38,39} (VASP) interfaced with the MedeA software environment. ⁴⁰ DFT calculations were based on the projector augmented wave method ⁴¹ using the Perdew–Burke–Ernzerhof (PBE) functional within the generalized gradient approximation. To account for the strong correlation of the electrons, an on-site Coulomb repulsion $U_{\rm eff} = U-J$ was added to the d orbitals of V within the rotationally invariant DFT + $U_{\rm eff}$ method of Dudarev et al. ⁴² In the present work, $U_{\rm eff}$ was set to 3.4 eV, which has been previously demonstrated to correctly describe VO₂, in particular the insulating behavior of the M1 phase. ^{43–46} Geometry optimizations were performed until forces were below 1 meV·Å⁻¹. All calculations used an energy cutoff of 500 eV, an electronic convergence set to 1 × 10^{-6} eV, and a k-point grid of 2 × 2 × 2.

2.7. Characterization. X-ray diffraction (XRD) was performed using a Rigaku MiniFlex 600 with a Cu Kα radiation source (λ = 1.5405 Å) operated at 40 mV and 30 mA. A JEOL FS100 field-emission scanning electron microscope (Peabody, MA, USA) equipped with an energy-dispersive X-ray spectroscopy (EDS) module was used for imaging and elemental mapping. A Thermo Fisher Talos F200x TEM was used for TEM imaging. FTIR-ATR measurements were carried out using a Shimadzu IRTracer-100 FTIR spectrophotometer. The scattering parameter of the antenna (S_{11}) was measured using an Agilent Technologies E5071C ENA series VNA with an operating frequency range of 300 kHz-20 GHz. Calibration of the VNA was performed using an 85052D mechanical calibration

kit (3.5 mm, 26.5 GHz, and 50 $\Omega)$ by Keysight. The switch printing was performed using a Voltera V-One PCB printer.

3. RESULTS AND DISCUSSION

Several structural phases of vanadium dioxide are reported in the literature, with the M, R, A, and B phases being the most common. The R phase comprises VO_6 octahedra at the corners and center of the lattice. The M phase can be subdivided into two monoclinic structures, M1 and M2. The former structure is analogous to an R phase cell doubled along the rutile c-axis (c_R) with zigzagging chains of tilted V–V dimers along c_R . In contrast, the M2 phase has half the chains as V–V dimers and half as unpaired V zigzags (Figure S2). S1–S3

The effect of Ge doping on the structure of VO₂ was evaluated using XRD. The amount of Ge added to the VO2 is calculated based on the intended doping percentage and defined as the Ge/(Ge + V) atomic ratio. Figure 1A shows the XRD patterns for pure VO₂(M1) after the hydrothermal synthesis, pure VO₂(M1) after annealing at 300 °C, pure VO₂(M1) after the second annealing at 700 °C, and targeted 1-5% Ge-doped VO₂. The pure VO₂(M1) diffraction pattern after annealing at 300 °C exhibits peaks that agree well with the M1 phase⁴⁹ (PDF #04-003-2035). The broadness of the peaks in the 300 °C sample is characteristic of nanoparticles, in agreement with the literature. ¹⁹ After annealing the VO₂(M1) at 700 °C, additional peaks appear in the diffraction pattern, attributed to minor peaks in the M1 phase. Furthermore, the broadness of the peaks is diminished; the new sharp peaks indicate improved crystallinity. Interestingly, the diffraction

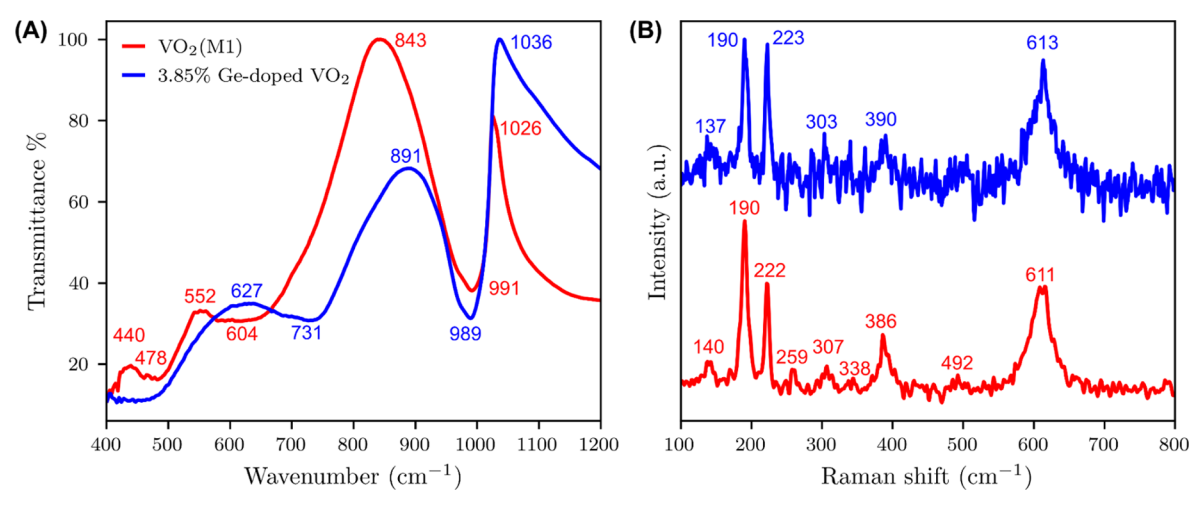


Figure 2. FTIR (A) and Raman (B) spectra of pure VO₂(M1) (red) and 3.85% Ge-doped VO₂ (blue).

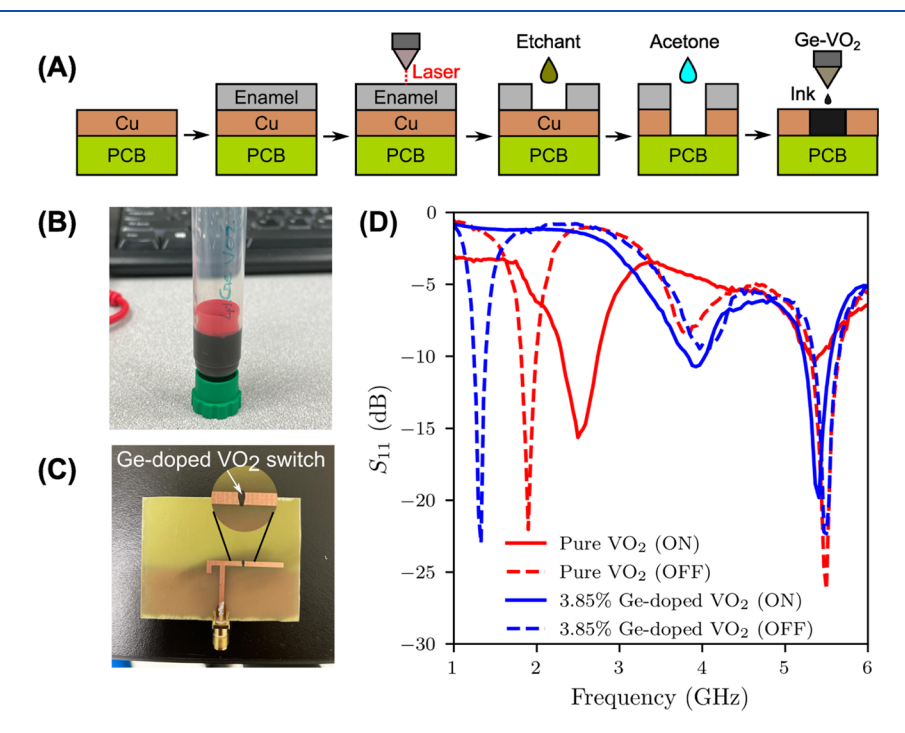


Figure 3. (A) Schematic of the antenna fabrication process by sequential laser etching and chemical etching. (B) Ge-doped VO_2 ink loaded into an ink cartridge for the Voltera V-One printer. (C) Image of final single-switch antenna. (D) VNA results of S_{11} of the pure VO_2 and 3.85% Ge-doped VO_2 antenna switches.

patterns of the Ge-doped ${\rm VO_2}$ samples appear nearly identical to that of pure ${\rm VO_2(M1)}$, suggesting substitutional doping. Although lower-valency elements tend to stabilize the intermediate M2 phase in ${\rm VO_2}$, such a phase does not appear in the diffraction pattern of the doped samples. This lack of an intermediate phase is consistent with previous works. 31,36 At 5.06% Ge doping, minor peaks appear at 14 and 28° and can be ascribed to oxygen-deficient vanadium oxide. 54 Overall, the sharp, definite peaks indicate high crystallinity, and the XRD pattern remains largely unperturbed by introducing Ge at the lower doping percentages.

The morphology of the undoped and Ge-doped VO_2 nanoparticles was examined by TEM and FE-SEM. TEM of the 3.85% Ge-doped VO_2 displays a particle size of 20–40 nm (Figure 1B). The *d*-spacing values of 3.16 and 2.36 Å, corresponding to the (001) and (-211) planes, respectively,

were calculated from the TEM image using ImageJ.⁵⁵ Pure VO₂ nanoparticles exhibit a peculiar aggregation pattern in hollow entities (rounded-edge cubes and spheres), as shown in Figure 1C. The relatively large particle sizes of the undoped VO₂ nanoparticles are a byproduct of the second annealing at 700 °C, supported by the narrow peak widths seen in the XRD patterns. The FE-SEM image of the Ge-doped samples (Figures 1D and S3) reveals aggregations of nanoparticles. The particle sizes of the Ge-doped VO₂ appear smaller than the undoped VO₂. The size reduction of Ge-doped VO₂ has been demonstrated in Ge-doped VO₂(M1) films made by Krammer et al.³¹ and Muller et al.^{16,17} and in other phases of Ge-doped VO₂.⁵⁶ It is hypothesized that the decrease in particle size for the doped samples is caused by an increase in the density of defect-induced nucleation sites.^{31,57}

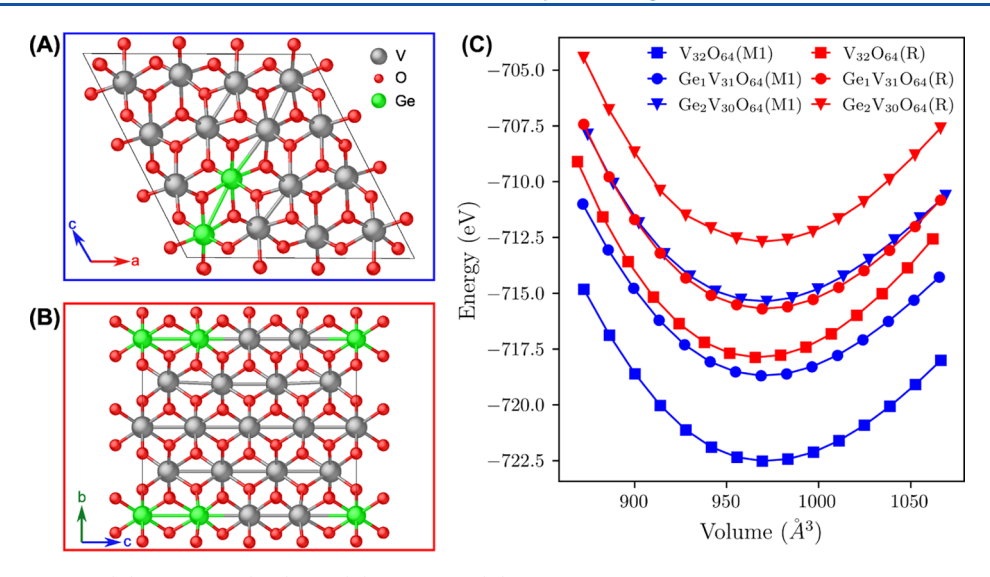


Figure 4. Crystal structures of (A) Ge₂V₃₀O₆₄(M1) and (B) Ge₂V₃₀O₆₄(R) after geometry optimization. The gray, red, and green spheres are the V, O, and Ge atoms. (C) Plot of fixed volume versus total energy for the structures considered.

Table 1. Structural Properties of VO₂ Phases as Predicted by PBE + U_{eff} and Equation-of-State Fitting

Material	$V(Å^3)$	a (Å)	b (Å)	c (Å)	α (°)	β (°)	γ (°)	B (GPa)
V ₃₂ O ₆₄ (M1)	972.70	10.816	9.274	10.924	90.0	117.4	90.0	193.20
$V_{32}O_{64}(R)$	967.44	9.318	9.318	11.142	90.0	90.0	90.0	223.94
$Ge_{1}V_{31}O_{64}$ (M1)	971.86	10.819	9.268	10.908	89.9	117.3	90.1	191.40
$Ge_{1}V_{31}O_{64}$ (R)	971.01	9.289	9.289	11.254	90.0	90.0	90.2	207.62
$Ge_{2}V_{30}O_{64}$ (M1)	969.51	10.820	9.255	10.888	89.7	117.2	90.3	195.88
$Ge_{2}V_{30}O_{64}$ (R)	969.32	9.273	9.273	11.274	90.0	90.0	90.1	213.15

Elemental mapping by EDS of Ge-doped VO2 reveals a homogeneous distribution, indicating that Ge has been well incorporated into the VO₂ nanoparticles, as shown in Figures 1E and S4. Area scans were performed on individual agglomerations to obtain an approximation of the doping percentage of Ge (Figure S5). The results and calculated doping percentage are summarized in Table S1. From the EDS area scans, the calculated doping percentage of Ge was determined to be 1.00, 2.24, 2.95, 3.85, and 5.06% for the targeted doping amounts of 1, 2, 3, 4, and 5%, respectively, relatively close to the intended values.

Postsynthesis FTIR analysis of pure VO₂(M1) and 3.85% Ge-doped VO₂ shows that there are no residual organic molecules adsorbed on the particle's surface. The FTIR spectra for both samples are shown in Figure 2A. The pure sample analysis resembles previously reported IR studies, 58-60 with the primary features being low transmission between 400 and 700 cm⁻¹ and leading to high transmission at 843 cm⁻¹. The bands of the Ge-doped sample appear broader than the pure sample and shift to higher wavenumbers. The strong signal at 989 and 991 cm $^{-1}$ may be attributed to short V=O bonds. ^{59,61} No other bands could be identified as belonging to organic molecules, demonstrating their removal post-hydrothermal annealing.

Figure 2B shows the Raman spectra for pure VO₂(M1) and 3.85% Ge-doped VO₂. VO₂(M1) has the representation Γ = $9A_g + 9B_g$, corresponding to 18 Raman active modes. The pure VO_2 sample features the following modes: six A_g modes at 140, 190, 222, 307, 386, and 611 cm⁻¹ and three B_g modes at 259, 338, and 492 cm⁻¹. These results agree with previous pure VO₂(M1) Raman studies. 62-64 The Raman spectrum for the 3.85% Ge-doped VO₂ shows similar peaks to those of the pure

sample at 137, 190, 303, 390, and 613 cm⁻¹. The spectrum for the Ge-doped sample exhibits a significantly lower signal-tonoise ratio, making identification of several Raman modes difficult. The absence of an intense Ge-Ge normal mode at 300 cm⁻¹⁶⁵ suggests that there is no remaining undissolved Ge in the lattice, indicative of full incorporation.

The antenna fabrication procedure is illustrated in Figure 3A. The nanoparticle ink is loaded into a cartridge for the Voltera printer (Figure 3B), and the final fabricated antenna is shown in Figure 3C. The performance of the single-switch Gedoped VO₂ antenna was determined using a VNA to acquire the scattering parameter S_{11} (return loss) in a single-port configuration. Two operating states are considered: at room temperature (OFF state) and heated to 100 °C (ON state). The results of VNA testing between 1 to 6 GHz are shown in Figure 3D. 3.85% Ge-doped VO₂ switches were chosen as candidates as the optimal performance was predicted to be near 4% doping.66 In the OFF state, the pure VO2 antenna operates at 1.90 GHz (-22.04 dB) and 5.50 GHz (-26.21 dB), while in the ON state, it operates at 2.50 GHz (-15.65)dB) and 5.35 GHz (-10.46 dB). For the Ge-doped VO₂ antennas, the operating frequencies are 1.33 GHz (-22.97 dB)and 5.50 GHz (-22.34 dB) in the OFF state and 3.93 GHz (-10.73 dB) and 5.41 GHz (-19.83 dB) in the ON state. The pure and Ge-doped VO₂ antennas show a clear change in the frequencies between the OFF and ON states due to the phase transition from $VO_2(M1)$ to $VO_2(R)$ of the switch. In the Gedoped VO₂ antennas, the frequencies shift significantly. Compared to pure VO₂, the Ge-doped VO₂ antennas show a change of -0.57 GHz (1.90 to 1.33 GHz) in the OFF state and +1.43 GHz (2.50 to 3.93 GHz) and +0.06 GHz (5.35 to 5.41 GHz) in the ON state. Accompanying these frequency shifts

ACS Applied Electronic Materials

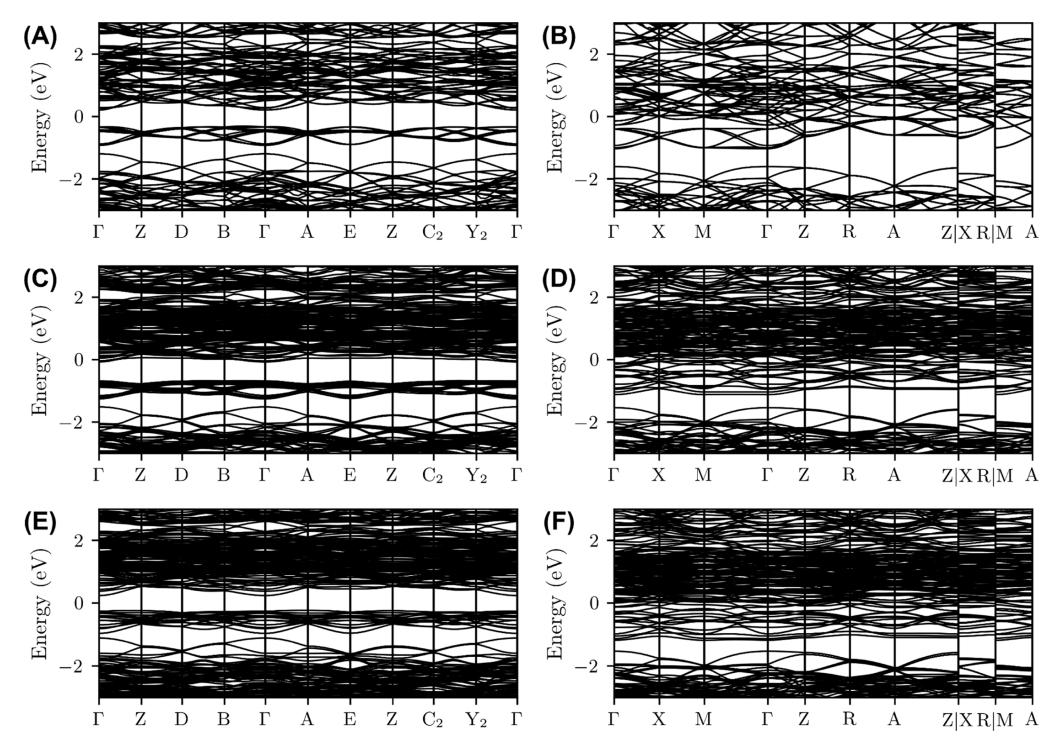


Figure 5. Electronic band structures of (A) $V_{32}O_{64}(M1)$, (B) $V_{32}O_{64}(R)$, (C) $Ge_1V_{31}O_{64}(M1)$, (D) $Ge_1V_{31}O_{64}(R)$, (E) $Ge_2V_{30}O_{64}(M1)$, and (F) $Ge_2V_{30}O_{64}(R)$ using PBE + U_{eff} . The Fermi energy is taken as the reference.

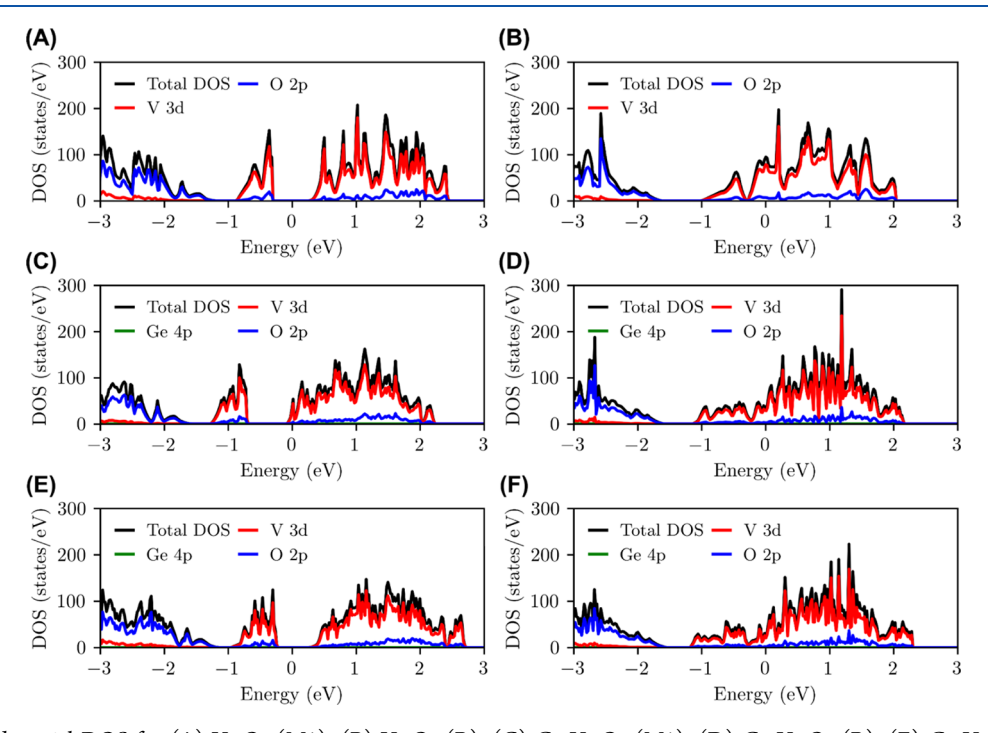


Figure 6. Total and partial DOS for (A) $V_{32}O_{64}(M1)$, (B) $V_{32}O_{64}(R)$, (C) $Ge_1V_{31}O_{64}(M1)$, (D) $Ge_1V_{31}O_{64}(R)$, (E) $Ge_2V_{30}O_{64}(M1)$, and (F) $Ge_2V_{30}O_{64}(R)$ using PBE + U_{eff} . The Fermi energy is taken as the reference.

are changes in the magnitude of S_{11} , mostly in the ON state, where there is a doubling of S_{11} at 5.41 GHz for the Ge-doped VO₂ antenna. These changes are likely due to the difference in conductive behavior by Ge doping.

To understand the effects of Ge doping on the optoelectronic properties and structure of VO_2 , first-principles calculations were carried out using DFT. $2 \times 2 \times 2$ and $2 \times 2 \times 4$ supercells were constructed for the M1 and R phases,

respectively, with doping simulated by the substitution of V atoms with Ge (Figure 4A,B). In this study, substitutional doping gives a Ge/V atom ratio of 1:31 and 2:30, corresponding to 3.13 and 6.25% Ge doping, respectively. Geometry optimization was carried out by computing a fixed volume versus free energy curve and fitting it to the Birch–Murnagham equation of state. The results of the geometry optimization are listed in Table 1. The volumes were

determined to be 972.70, 967.44, 971.86, 971.01, 969.51, and 969.32 Å³ for $V_{32}O_{64}(M1)$, $V_{32}O_{64}(R)$, $Ge_1V_{31}O_{64}(M1)$, $Ge_1V_{31}O_{64}(R)$, $Ge_2V_{30}O_{64}(M1)$, and $Ge_2V_{30}O_{64}(R)$ supercells, respectively. By substituting V with Ge, the supercell volumes change at most by -0.33% (M1) and +0.37% (R). Distortion in the lattice can be seen as deviations in the lattice angles of the doped supercells from their undoped values, resulting in a lowering of symmetry. The final lattice parameters of the M1 phase supercells were determined to be 10.816, 10.819, and 10.820 Å (a), 9.274, 9.268, and 9.255 Å (b), and 10.924, 10.908, and 10.888 Å (c) for $V_{32}O_{64}$ (M1), $Ge_1V_{31}O_{64}$ (M1), and Ge₂V₃₀O₆₄ (M1), respectively. The optimized lattice parameters a and c for the R phase supercells were 9.318 and 11.142 Å for $V_{32}O_{64}$ (R), 9.289 and 11.254 Å for $Ge_1V_{31}O_{64}$ (R), and 9.273 and 11.274 Å for $Ge_2V_{30}O_{64}$ (R). As calculated from the equation-of-state fitting, the bulk moduli were 193.20, 223.94, 191.40, 207.62, 195.88, and 213.15 GPa for $V_{32}O_{64}(M1)$, $V_{32}O_{64}(R)$, $Ge_1V_{31}O_{64}(M1)$, $Ge_1V_{31}O_{64}(R)$, Ge₂V₃₀O₆₄(M1), and Ge₂V₃₀O₆₄(R), respectively. Figure 4C shows that the free energies of $V_{32}O_{64}(M1)$, $Ge_1V_{31}O_{64}(M1)$, and $Ge_2V_{30}O_{64}(M1)$ are lower than their R phase counterparts, indicating that the M1 phase is more stable than the R phase regardless of the inclusion of a Ge dopant.

The effects of Ge doping on the electronic structure can be readily found by calculating the electronic density of states and band structures. The band structures of V₃₂O₆₄(M1) and $V_{32}O_{64}(R)$, both pure and Ge-doped, are shown in Figure 5. The high-symmetry paths were determined using SeeK-path⁶⁷ on the primitive cells of the $VO_2(M1)$ and $VO_2(R)$. In the cases of $V_{32}O_{64}(M1)$ and $V_{32}O_{64}(R)$, the semiconducting and metallic behaviors are reproduced, respectively. The fundamental band gap of V₃₂O₆₄(M1), Ge₁V₃₁O₆₄(M1), and $Ge_2V_{30}O_{64}(M1)$ was calculated to be 0.518, 0.597, and 0.471 eV, respectively, comparable to that reported in previous experimental studies. 68-70 Notably, the band gap is significantly reduced at higher doping percentages, consistent with other theoretical studies.⁶⁶ An upward shift in the Fermi energy is seen for Ge₁V₃₁O₆₄(M1) due to an unpaired electron; however, this shifts back into the middle of the band gap for Ge₂V₃₀O₆₄(M1). In contrast, the R phase band structures remain unchanged. The total and partial density of states (DOS) for each structure are shown in Figure 6. As seen from the band structures, the significant features of the pure VO₂ DOS prevail in the Ge-doped VO₂ DOS. The valence band near the Fermi level and the bottom of the conduction band of V₃₂O₆₄(M1) and Ge₁V₃₁O₆₄(M1) are dominated by V 3d states with a minor number of O 2p states. For $V_{32}O_{64}(R)$ and $Ge_1V_{31}O_{64}(R)$, the O 2p states comprise most of the valence band, while the V 3d states dominate the conduction band. The major contributions to the DOS for $Ge_2V_{30}O_{64}(M1)$ and $Ge_2V_{30}O_{64}(R)$ are identical to the previous structures, with only minor differences in the intensities of the V 3d and O 2p states. It is important to note that the presence of Ge (in the form of its 4p states) is very low near the band edges compared to the overall characteristics of the DOS. This lack of Ge states in the DOS was previously reported,³⁶ concluding that the structural distortions of the parent VO2 structure contribute to changes in $T_{\rm MIT}$ of Ge-doped VO₂ instead of electronic contributions. However, more sophisticated calculations⁶⁶ utilizing noncollinear spin DFT demonstrated minor yet present Ge states in their DOS calculations. Therefore, computational methods

should account for magnetism to yield a more accurate picture of the Ge dopant's effect.

4. CONCLUSIONS

Ge-doped VO₂ nanoparticles with controlled doping percentage were successfully synthesized via a hydrothermal route followed by postsynthesis annealing. Characterization via XRD results shows a monoclinic phase (M1) of VO₂ for pure and Ge-doped powders, further validated by Raman spectroscopy. Little change in the M1 phase XRD is seen in the Ge-doped samples at below 5% doping, consistent with the literature. The nanocrystalline size is confirmed by TEM, which confirms the nanocrystal morphology of the Ge-doped VO2, and FE-SEM and EDS show Ge uniformly distributed throughout the VO₂ nanocrystals. Nanoparticle inks were produced from the Ge-doped VO₂ and used to fabricate ON/OFF frequency switches in a simple antenna design. VNA results demonstrated that the switches performed as intended, undergoing changes in the operating frequencies upon heating. Testing also shows frequency shifts in the operating frequencies between the pure VO₂ and Ge-doped VO₂ antennas, likely due to the difference in conductive properties resulting from Ge doping. DFT simulations predict that substituting Ge into a V site of the crystal structure not only distorts the lattice but reduces the band gap at higher doping percentages. This change does not appear to be directly attributed to Ge orbitals but rather to lattice distortion.

ASSOCIATED CONTENT

Supporting Information

The Supporting Information is available free of charge at https://pubs.acs.org/doi/10.1021/acsaelm.3c00498.

Key steps in the fabrication of the single-switch antennas; unit cells of $VO_2(M1)$, $VO_2(R)$, and $VO_2(M2)$; SEM images of pure VO_2 , 1.00, 2.24, 2.95, 3.85, and 5.06% Ge-doped VO_2 ; elemental mapping by EDS of 1.00, 2.24, 2.95, 3.85, and 5.06% Ge-doped VO_2 nanoparticles; EDS results for area scan of 1.00, 2.24, 2.95, 3.85, and 5.06% Ge-doped VO_2 ; design and dimensions of single-switch Ge-doped VO_2 antenna; and elemental analysis of 1–5% Ge-doped VO_2 by EDS (PDF)

AUTHOR INFORMATION

Corresponding Author

Daniela R. Radu — Department of Mechanical and Materials Engineering, Florida International University, Miami, Florida 33174, United States; orcid.org/0000-0001-6833-5825; Email: dradu@fiu.edu

Authors

Roberto Prado-Rivera — Department of Mechanical and Materials Engineering, Florida International University, Miami, Florida 33174, United States; orcid.org/0000-0002-3376-6673

Cheng-Yu Lai — Department of Mechanical and Materials Engineering, Florida International University, Miami, Florida 33174, United States; ◎ orcid.org/0000-0002-8931-5601

Mujtaba Ali Haqqani Mohammed — Department of Mechanical and Materials Engineering, Florida International University, Miami, Florida 33174, United States

- Chen-Yu Chang Department of Mechanical and Materials Engineering, Florida International University, Miami, Florida 33174, United States; orcid.org/0000-0001-5253-1813
- Faizan Syed Department of Mechanical and Materials Engineering, Florida International University, Miami, Florida 33174, United States

Complete contact information is available at: https://pubs.acs.org/10.1021/acsaelm.3c00498

Author Contributions

The manuscript was written through contributions of all authors. All authors have given approval to the final version of the manuscript.

Funding

This work was supported in part by the ONR award no. N00014-20-1-2539; NASA awards 80NSSC19M0201, 80NSSC21M0310, and 80NSSC20K1462; and in part by the National Science Foundation award DMR-2122078.

Notes

The authors declare no competing financial interest.

ACKNOWLEDGMENTS

The authors acknowledge Dr. Elias Alwan for helpful discussions regarding antenna parameter measurements.

REFERENCES

- (1) Adler, D. Mechanisms for Metal-Nonmental Transitions in Transition-Metal Oxides and Sulfides. *Rev. Mod. Phys.* **1968**, *40*, 714–736
- (2) Slater, J. C. Magnetic Effects and the Hartree-Fock Equation. *Phys. Rev.* 1951, 82, 538-541.
- (3) Mott, N. F.; Zinamon, Z. The Metal-Nonmetal Transition. *Rep. Prog. Phys.* **1970**, 33, 881–940.
- (4) Imada, M.; Fujimori, A.; Tokura, Y. Metal-Insulator Transitions. Rev. Mod. Phys. 1998, 70, 1039–1263.
- (5) Demeter, M.; Neumann, M.; Reichelt, W. Mixed-Valence Vanadium Oxides Studied by XPS. Surf. Sci. 2000, 454–456, 41–44.
- (6) Fisher, B.; Patlagan, L.; Chashka, K. B.; Makarov, C.; Reisner, G. M. V3O5: Insulator-Metal Transition and Electric-Field-Induced Resistive-Switching. Appl. Phys. Lett. 2016, 109, 103501.
- (7) Fletcher, E. R. A.; Higashi, K.; Kalcheim, Y.; Kageyama, H.; Frandsen, B. A. Uniform Structural Phase Transition in V2O3 Without Short-Range Distortions of the Local Structure. *Phys. Rev. B* **2021**, *104*, 184115.
- (8) Goodenough, J. Metallic Oxides. *Prog. Solid State Chem.* **1971**, *5*, 145–399.
- (9) Kalcheim, Y.; Butakov, N.; Vargas, N. M.; Lee, M. H.; Del Valle, J.; Trastoy, J.; Salev, P.; Schuller, J.; Schuller, I. K. Robust Coupling between Structural and Electronic Transitions in a Mott Material. *Phys. Rev. Lett.* **2019**, *122*, 057601.
- (10) Kumar, N.; Rua, A.; Lu, J.; Fernandez, F.; Lysenko, S. Ultrafast Excited-State Dynamics of V3O5 as a Signature of a Photoinduced Insulator-Metal Phase Transition. *Phys. Rev. Lett.* **2017**, *119*, 057602.
- (11) Morin, F. J. Oxides Which Show a Metal-to-Insulator Transition at the Neel Temperature. *Phys. Rev. Lett.* **1959**, *3*, 34–36.
- (12) Cui, Y.; Ke, Y.; Liu, C.; Chen, Z.; Wang, N.; Zhang, L.; Zhou, Y.; Wang, S.; Gao, Y.; Long, Y. Thermochromic VO2 for Energy-Efficient Smart Windows. *Joule* 2018, 2, 1707–1746.
- (13) Xu, F.; Cao, X.; Luo, H.; Jin, P. Recent Advances in VO2-Based Thermochromic Composites for Smart Windows. *J. Mater. Chem. C* **2018**, *6*, 1903–1919.
- (14) Liang, J.; Lou, Q.; Wu, W.; Wang, K.; Xuan, C. NO2 Gas Sensing Performance of a VO2(B) Ultrathin Vertical Nanosheet

- Array: Experimental and DFT Investigation. Acs Appl Mater Inter 2021, 13, 31968-31977.
- (15) Khan, Z.; Singh, P.; Ansari, S. A.; Manippady, S. R.; Jaiswal, A.; Saxena, M. VO2 Nanostructures for Batteries and Supercapacitors: A Review. *Small* **2021**, *17*, No. e2006651.
- (16) Muller, A.; Khadar, R. A.; Abel, T.; Negm, N.; Rosca, T.; Krammer, A.; Cavalieri, M.; Schueler, A.; Qaderi, F.; Bolten, J.; et al. Radio-Frequency Characteristics of Ge-Doped Vanadium Dioxide Thin Films with Increased Transition Temperature. ACS Appl. Electron. Mater. 2020, 2, 1263–1272.
- (17) Muller, A. A.; Khadar, R.; Niang, K. M.; Bai, G.; Matioli, E.; Robertson, J.; Ionescu, A. M. Radio Frequency Temperature Transducers Based on Insulator-Metal Phase Transition in VO2 and Ge-Doped VO2 ALD Thin Films. In 2021 21st International Conference on Solid-State Sensors, Actuators and Microsystems (Transducers); IEEE: Orlando, FL, USA, 2021-06-20, 2021.
- (18) Anagnostou, D. E.; Torres, D.; Teeslink, T. S.; Sepulveda, N. Vanadium Dioxide for Reconfigurable Antennas and Microwave Devices: Enabling RF Reconfigurability Through Smart Materials. *IEEE Antennas Propag. Mag.* **2020**, *62*, 58–73.
- (19) Vaseem, M.; Zhen, S.; Yang, S.; Li, W.; Shamim, A. Development of VO2-Nanoparticle-Based Metal-Insulator Transition Electronic Ink. *Adv. Electron. Mater.* **2019**, *5*, 1800949.
- (20) Yang, S.; Vaseem, M.; Shamim, A. Fully Inkjet-Printed VO2-Based Radio-Frequency Switches for Flexible Reconfigurable Components. *Adv. Mater. Technol.* **2019**, *4*, 1800276.
- (21) Cao, X.; Chang, T.; Shao, Z.; Xu, F.; Luo, H.; Jin, P. Challenges and Opportunities toward Real Application of VO2-Based Smart Glazing. *Matter-Us* **2020**, *2*, 862–881.
- (22) Tang, C.; Georgopoulos, P.; Fine, M. E.; Cohen, J. B.; Nygren, M.; Knapp, G. S.; Aldred, A. Local Atomic and Electronic Arrangements in WxV1-xO2. *Phys. Rev. B. Condens. Matter.* **1985**, 31, 1000–1011.
- (23) Romanyuk, A.; Steiner, R.; Marot, L.; Oelhafen, P. Temperature-Induced Metal-Semiconductor Transition in W-Doped VO2 Films Studied by Photoelectron Spectroscopy. *Sol. Energ. Mat. Sol. C* **2007**, *91*, 1831–1835.
- (24) Takami, H.; Kawatani, K.; Kanki, T.; Tanaka, H. High Temperature-Coefficient of Resistance at Room Temperature in W-Doped VO2 Thin Films on Al2O3 Substrate and Their Thickness Dependence. *Jpn. J. of Appl. Phys.* **2011**, *50*, 055804.
- (25) Wu, T.-L.; Whittaker, L.; Banerjee, S.; Sambandamurthy, G. Temperature and Voltage Driven Tunable Metal-Insulator Transition in Individual WxV1-xO2 Nanowires. *Phys. Rev. B* **2011**, 83, 073101.
- (26) Gu, Q.; Falk, A.; Wu, J.; Ouyang, L.; Park, H. Current-Driven Phase Oscillation and Domain-Wall Propagation in $W_xV_{1-x}O_2$ Nanobeams. *Nano Lett.* **2007**, *7*, 363–366.
- (27) Krammer, A.; Bouvard, O.; Schüler, A. Study of Si Doped VO2 Thin Films for Solar Thermal Applications. *Energy Procedia* **2017**, 122, 745–750.
- (28) Tan, X.; Liu, W.; Long, R.; Zhang, X.; Yao, T.; Liu, Q.; Sun, Z.; Cao, Y.; Wei, S. Symmetry-Controlled Structural Phase Transition Temperature in Chromium-Doped Vanadium Dioxide. *J. Phys. Chem.* C 2016, 120, 28163–28168.
- (29) Futaki, H.; Kobayashi, K.; Aoki, M.; Shimoda, T.; Yamada, E.; Narita, K. Thermistor Composition Containing Vanadium Dioxide. U.S. Patent 3,402,131 A, 1968.
- (30) Eastwood, H. K.; Noval, B. A. Method of Producing Thin Film Devices of Doped Vanadium Oxide Material. U.S. Patent 3,899,407 A, 1975.
- (31) Krammer, A.; Magrez, A.; Vitale, W. A.; Mocny, P.; Jeanneret, P.; Guibert, E.; Whitlow, H. J.; Ionescu, A. M.; Schüler, A. Elevated Transition Temperature in Ge Doped VO2 Thin Films. *J. Appl. Phys.* **2017**, *122*, 045304.
- (32) Lu, H.; Guo, Y.; Robertson, J. Electronic Structure of Metallic and Insulating Phases of Vanadium Dioxide and its Oxide Alloys. *Phys. Rev. Mater.* **2019**, *3*, 094603.

- (33) Chiang, H. C.; Wang, M. H.; Ueng, C. H. Synthesis and Structure of diaquabis(glycolato-O,O")germanium(IV). *Acta Cryst* **1993**, *49*, 244–246.
- (34) Liu, M.; Berg, D. M.; Hwang, P.-Y.; Lai, C.-Y.; Stone, K. H.; Babbe, F.; Dobson, K. D.; Radu, D. R. The Promise of Solution-Processed Fe2GeS4 Thin Films in Iron Chalcogenide Photovoltaics. *J. Mater. Sci.* **2018**, *53*, 7725–7734.
- (35) Zou, J.; Xiao, L.; Zhu, L.; Chen, X. One-Step Rapid Hydrothermal Synthesis of Monoclinic VO2 Nanoparticles With High Precursors Concentration. *J. Sol-Gel Sci. Technol.* **2019**, *91*, 302–309
- (36) Wang, L.; Hao, Y.-Q.; Ma, W.; Liang, S. Improving Phase Transition Temperature of VO2 via Ge Doping: A Combined Experimental and Theoretical Study. *Rare Met* **2021**, *40*, 1337–1346.
- (37) Vaseem, M.; Su, Z.; Yang, S.; Shamim, A. Fully Printed Flexible and Reconfigurable Antenna With Novel Phase Change VO2 Ink Based Switch. In *International Flexible Electronics Technology Conference (IFETC)*; IEEE: Ottawa, ON, Canada, 2018-08-01, 2018: pp 1-2
- (38) Kresse, G.; Furthmüller, J. Efficiency of ab-initio total energy calculations for metals and semiconductors using a plane-wave basis set. *Comp. Mater. Sci.* **1996**, *6*, 15–50.
- (39) Kresse, G.; Furthmuller, J. Efficient Iterative Schemes for Ab Initio Total-Energy Calculations Using a Plane-Wave Basis Set. *Phys. Rev. B. Condens. Matter.* **1996**, *54*, 11169–11186.
- (40) Medea-Materials Exploration and Design Analysis; Materials Design, Inc.: 2021.
- (41) Kresse, G.; Joubert, D. From Ultrasoft Pseudopotentials to the Projector Augmented-Wave Method. *Phys. Rev. B* **1999**, *59*, 1758–1775.
- (42) Dudarev, S. L.; Botton, G. A.; Savrasov, S. Y.; Humphreys, C. J.; Sutton, A. P. Electron-Energy-Loss Spectra and the Structural Stability of Nickel Oxide: An LSDA+U Study. *Phys. Rev. B* **1998**, *57*, 1505–1509.
- (43) Stahl, B.; Bredow, T. Critical Assessment of the DFT + U Approach for the Prediction of Vanadium Dioxide Properties. *J. Comput. Chem.* **2020**, *41*, 258–265.
- (44) Cui, Y.; Liu, B.; Chen, L.; Luo, H.; Gao, Y. Formation Energies of Intrinsic Point Defects in Monoclinic VO2 Studied By First-Principles Calculations. *AIP Advances* **2016**, *6*, 105301.
- (45) Chen, L.; Wang, X.; Shi, S.; Cui, Y.; Luo, H.; Gao, Y. Tuning the Work Function of VO2(100) Surface by Ag Adsorption and Incorporation: Insights from First-Principles Calculations. *Appl. Surf. Sci.* **2016**, 367, 507–517.
- (46) Biermann, S.; Poteryaev, A.; Lichtenstein, A. I.; Georges, A. Dynamical Singlets and Correlation-Assisted Peierls Transition in VO2. *Phys. Rev. Lett.* **2005**, *94*, 026404.
- (47) Westman, S.; Lindqvist, I.; Sparrman, B.; Nielsen, G. B.; Nord, H.; Jart, A. Note on a Phase Transition in VO2. *Acta Chem. Scand.* **1961**, *15*, 217.
- (48) McWhan, D. B.; Marezio, M.; Remeika, J. P.; Dernier, P. D. X-Ray Diffraction Study of Metallic VO2. *Phys. Rev. B* **1974**, *10*, 490–495.
- (49) Longo, J. M.; Kierkegaard, P.; Ballhausen, C. J.; Ragnarsson, U.; Rasmussen, S. E.; Sunde, E.; Sørensen, N. A. A Refinement of the Structure of VO2. *Acta Chem. Scand.* **1970**, *24*, 420–426.
- (50) Andersson, G.; Parck, C.; Ulfvarson, U.; Stenhagen, E.; Thorell, B. Studies on Vanadium Oxides. II. The Crystal Structure of Vanadium Dioxide. *Acta Chem. Scand.* **1956**, *10*, 623–628.
- (51) Marezio, M.; McWhan, D. B.; Remeika, J. P.; Dernier, P. D. Structural Aspects of the Metal-Insulator Transitions in Cr-Doped VO2. *Phys. Rev. B* **1972**, *5*, 2541–2551.
- (52) Pouget, J. P.; Launois, H.; Rice, T. M.; Dernier, P.; Gossard, A.; Villeneuve, G.; Hagenmuller, P. Dimerization of a Linear Heisenberg Chain in the Insulating Phases of V1-xCrxO2. *Phy. Rev. B.* **1974**, *10*, 1801–1815
- (53) Pouget, J. P.; Launois, H.; D'Haenens, J. P.; Merenda, P.; Rice, T. M. Electron Localization Induced by Uniaxial Stress in Pure VO2. *Phys. Rev. Lett.* **1975**, *35*, 873–875.

ı

- (54) Davydov, D. A.; Gusev, A. I. The Disorder-Order Transition in Cubic Vanadium Monoxide With Vacancies in the Metal Sublattice. *J. Exp. Theor. Phys.* **2009**, *108*, 267–278.
- (55) Schneider, C. A.; Rasband, W. S.; Eliceiri, K. W. NIH Image to ImageJ: 25 Years of Image Analysis. *Nat. Methods* **2012**, *9*, 671–675.
- (56) Saini, M.; Malik, R.; Lata, S.; Saini, B.; Kumar, P.; Dehiya, B. S.; Seo, H.-K.; Umar, A. Synthesis and Electrochemical Properties of Ge4+ Ions-Modified VO2(paramontroseite). *J. Mater. Sci.: Mater. Electron.* **2020**, *31*, 3795–3802.
- (57) Du, J.; Gao, Y.; Luo, H.; Kang, L.; Zhang, Z.; Chen, Z.; Cao, C. Significant Changes in Phase-Transition Hysteresis for Ti-doped VO2 Films Prepared by Polymer-Assisted Deposition. *Sol. Energ. Mat. Sol.* C **2011**, 95, 469–475.
- (58) Hewston, T. A.; Nadler, M. P. Variable-Temperature Infrared Spectra of VO2. *J. Sol. State Chem.* 1987, 71, 278–281.
- (59) Botto, I. L.; Vassallo, M. B.; Baran, E. J.; Minelli, G. IR spectra of VO2 and V2O3. *Mater. Chem. Phys.* **1997**, *50*, 267–270.
- (60) Zheng, C. M.; Zhang, X. M.; Zhang, J. H.; Liao, K. R. Preparation and Characterization of VO2 Nanopowders. *J. Solid State Chem.* **2001**, *156*, 274–280.
- (61) Beattie, I. R.; Gilson, T. R. Oxide Phonon Spectra. *J. Chem. Soc.* A **1969**, 2322–2327.
- (62) Shvets, P.; Dikaya, O.; Maksimova, K.; Goikhman, A. A Review of Raman Spectroscopy of Vanadium Oxides. *J. Raman Spectrosc.* **2019**, *50*, 1226–1244.
- (63) Pan, M.; Liu, J.; Zhong, H. M.; Wang, S. W.; Li, Z. F.; Chen, X. H.; Lu, W. Raman Study of the Phase Transition in VO2 Thin Films. *J. Cryst. Growth* **2004**, *268*, 178–183.
- (64) Schilbe, P. Raman Scattering in VO2. *Physica B* **2002**, 316–317, 600–602.
- (65) Ertas Uslu, M.; Misirlioglu, I. B.; Sendur, K. Crossover of Spectral Reflectance Lineshapes in Ge-Doped VO2 Thin Films. *Opt. Mater.* **2020**, *104*, 109890.
- (66) Lu, H.; Clark, S.; Guo, Y.; Robertson, J. Modelling the Enthalpy Change and Transition Temperature Dependence of the Metal-Insulator Transition in Pure and Doped Vanadium Dioxide. *Phys. Chem. Chem. Phys.* **2020**, *22*, 13474–13478.
- (67) Hinuma, Y.; Pizzi, G.; Kumagai, Y.; Oba, F.; Tanaka, I. Band Structure Diagram Paths Based On Crystallography. *Comp. Mater. Sci.* **2017**, *128*, 140–184.
- (68) Lee, S.; Meyer, T. L.; Sohn, C.; Lee, D.; Nichols, J.; Lee, D.; Seo, S. S. A.; Freeland, J. W.; Noh, T. W.; Lee, H. N. Electronic Structure and Insulating Gap in Epitaxial VO2 Polymorphs. *APL Mater.* **2015**, *3*, 126109.
- (69) Qazilbash, M. M.; Brehm, M.; Chae, B. G.; Ho, P. C.; Andreev, G. O.; Kim, B. J.; Yun, S. J.; Balatsky, A. V.; Maple, M. B.; Keilmann, F.; et al. Mott Transition in VO2 Revealed by Infrared Spectroscopy and Nano-Imaging. *Science* **2007**, *318*, 1750–1753.
- (70) Jiang, M.; Li, Y.; Li, S.; Zhou, H.; Cao, X.; Bao, S.; Gao, Y.; Luo, H.; Jin, P. Room Temperature Optical Constants and Band Gap Evolution of Phase Pure M1-VO2 Thin Films Deposited at Different Oxygen Partial Pressures by Reactive Magnetron Sputtering. *J. Nanomater.* **2014**, *2014*, 1–6.